ACS OMEGA

Article

Cite This: ACS Omega 2018, 3, 8440−8450

http://pubs.acs.org/journal/acsodf

Combined Structural, Chemometric, and Electrochemical Investigation of Vertically Aligned TiO_2 Nanotubes for Na-ion Batteries

Federico Bella,*[,†] Ana B. Muñoz-García,[‡] Francesca Colò,[†] Giuseppina Meligrana,[†] Andrea Lamberti,[§] Matteo Destro,[∥] Michele Pavone,[⊥] and Claudio Gerbaldi*[,†]

[†]GAME Lab, Department of Applied Science and Technology—DISAT, and [§]MPMNT Group, Department of Applied Science and Technology—DISAT, Politecnico di Torino, Corso Duca degli Abruzzi 24, 10129 Torino, Italy

[‡]Department of Physics "E. Pancini" and [⊥]Department of Chemical Sciences, University of Naples Federico II, Comp. Univ. Monte Sant'Angelo, Via Cintia 21, 80126 Napoli, Italy

[∥]LITHOPS Batteries S.r.l., Via della Rocca 27, 10123 Torino, Italy

ABSTRACT: In the challenging scenario of anode materials for sodium-ion batteries, TiO_2 nanotubes could represent a winning choice in terms of cost, scalability of the preparation procedure, and long-term stability upon reversible operation in electrochemical cells. In this work, a detailed physicochemical, computational, and electrochemical characterization is carried out on TiO_2 nanotubes synthesized by varying growth time and heat treatment, viz. the two most significant experimental parameters during preparation. A chemometric approach is proposed to obtain a concrete and solid multivariate analysis of sodium battery electrode materials. Such a statistical approach, combined with prolonged galvanostatic cycling and density functional theory analysis, allows identifying anatase at high growth time as the TiO_2 polymorph of choice as an anode material, thus creating a benchmark for sodium-ion batteries, which currently took the center stage of the research in the field of energy storage systems from renewables.

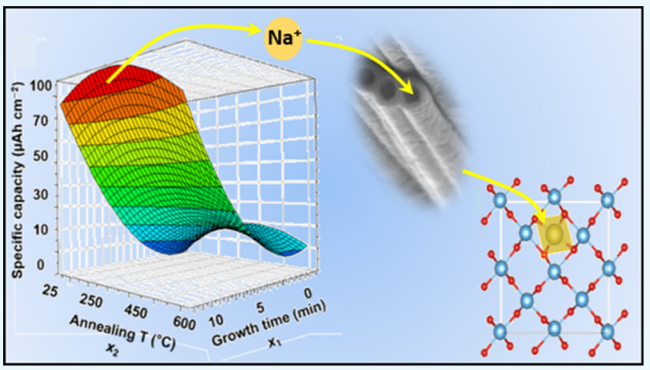

1. INTRODUCTION

Current tremendously growing energy demand is pushing forward the pursuit of high-performing, cost-effective, safe and environmentally friendly energy conversion and storage systems. Indeed, electricity generated from renewable sources represents an oasis in the future to effectively meet the demand for energy supply systems characterized by as low as possible carbon footprint.[1] However, renewable sources, such as wind, solar, tidal, biomass, and geothermal, are all inherently intermittent and, often, widely scattered into isolated large-scale facilities around the globe.[2] The best way to exploit these energy resources for practical human needs is to set up smart and efficient systems to store the energy they produce.[3−7] To this purpose, secondary batteries represent a viable solution for the integration of renewable plants into the grid and will play a fundamental role to guarantee a brighter and cleaner environment for future generations.[8−12]

Whereas Li-ion batteries (LIBs) offer the highest energy density among present battery technologies,[13−17] still an amount of open challenges remains to be faced, particularly the reduced availability of global lithium resources, which are also mainly concentrated in remote and/or politically sensitive areas,[18−21] and its increasing cost due to the rising demand for smart high energy/power density storage devices. Indeed, people are now starting to consider lithium as "the new gold",[22] as its price recently soared 300%.[23] In this respect, sodium is rapidly emerging as an alternative light metal for batteries: it is cheap and very abundant and has a uniform geographical distribution.[24−26] Its redox potential is −2.71 V versus standard hydrogen electrode (vs −3.04 V of lithium); moreover, Na^+ is heavier (23 vs 6.9 g mol^{-1}) and larger (97 vs 68 pm) than Li^+. This means that—when sodium is considered—a small penalty has to be paid in terms of overall cell operating potential and gravimetric/volumetric energy densities, but it is anyway much more appealing than lithium when widespread, low-cost, and large-scale energy storage systems (ESSs) have to be implemented.[27,28] For all of these reasons, the investigation of materials for sodium-ion batteries (NIBs), along with the correct understanding of their electrochemical characteristics, has recently become hot topics within the scientific community.[29−33]

Received: May 24, 2018
Accepted: July 18, 2018
Published: July 31, 2018

DOI: 10.1021/acsomega.8b01117
ACS Omega 2018, 3, 8440−8450

One of the main issues of NIB technology concerns the selection of suitable anode materials.[34−36] Graphite—the commercial choice anode for LIBs—cannot be used in NIBs because of its extremely low performance. Indeed, while Li^+ ions are readily inserted into graphite with a final stoichiometry of LiC_6 (accounting for a theoretical specific capacity of 372 mAh g^{-1}), only a very little amount of Na^+ ions can be intercalated into graphite.[37,38] Such a limited capacity can be explained from a thermodynamic viewpoint, being related to Na plating on the carbon surface before forming the graphite intercalation compounds.[39]

The lack of low-voltage metal oxide anodes assuring reversible storage of sodium ions at room temperature and for a sufficient amount of cycles[40,41] can be justified by the large ionic radius of Na^+, the insertion of which in nanostructured electrodes requires substantial distortion of the metal oxide lattice.[42] To this purpose, titanium dioxide (TiO_2) could represent a viable solution, being a stable, safe, inexpensive, nontoxic, and abundant semiconductor, able to intercalate alkali ions at moderate potential values with specific capacities comparable to graphite anodes in LIBs. Given these features, TiO_2 would clearly represent an interesting material to be investigated as the anode for NIBs,[43−45] as first reported by Xu et al.[46] and Usui et al.[47] Unfortunately, it shows intrinsic low electronic conductivity, which accounts for relatively poor rate capability. As a viable solution, the use of one-dimensional TiO_2 nanostructures (i.e., nanowires, nanorods, and nanotubes) provides shorter electron diffusion paths and improved conductivity values.[48,49] Among the number of approaches proposed by the scientific community for the preparation of ordered TiO_2 nanostructures,[50] anodic oxidation stands out as a well-established technique that allows large area samples, along with the obtainment of uniform nanotubular arrays (namely, TiO_2 NTs) characterized by interesting characteristics for various energy-related applications and relatively high specific surface.[51−53] Other two advantages of TiO_2 NTs are relevant in the battery field: (i) regularly aligned inner nanopores may provide preferential pathways for the fast diffusion of the electrolyte, which can also thoroughly wet the active material surface; (ii) the growth process can be performed onto conducting flexible substrates (e.g., Ti foil), thus avoiding the use of binders and electronic conductivity enhancers, which clearly influence the overall cell energy density.[54]

Despite some research groups have recently proposed TiO_2 NTs as the anode for NIBs, the scientific community does not agree on some fundamental aspects as to which is the best polymorph (e.g., amorphous or crystalline anatase/rutile) in terms of overall capacity output and/or long-term performance and which kind of modifications occur to the nanostructure during cell operation.[55,56]

Very recently, we proposed a possible explanation for the different electrochemical behavior of the amorphous and anatase phases of TiO_2 nanotubes,[57] demonstrating the superior behavior of the latter upon long-term reversible cycling in lab-scale sodium cells. Here, we thoroughly investigate how the different experimental parameters, related to the growth time of the nanostructures by anodic oxidation and to different structural characteristics obtained upon annealing at different temperatures, influence the overall electrochemical response of the material, thus allowing to define the best performing polymorph. In addition, most of the research works published in the NIBs field consist in monovariate analysis; however, such a procedure often leads to error when interactions between the variables occur. As a result, we propose here an experimental design that simultaneously studies different variables to obtain not only an empirical mathematical equation for the considered factors but also a response map useful to consider the influence of all the parameters. As a result, a systematic approach to identify suitable active materials and properly optimize them to develop highly efficient sodium-based ESSs is presented.

In this work, we aim at identifying the best TiO_2 polymorph for NIBs, by means of a solid and combined experimental, computational, and statistical approaches.

2. RESULTS AND DISCUSSION

2.1. Morphological and Structural Characterization.

X-ray diffraction (XRD) and field emission scanning electron microscopy (FESEM) analyses were performed on the different fresh samples as well as at the end of the galvanostatic cycling test. XRD profiles of the different anodized samples, that is, pristine amorphous (nonthermally treated, namely TiO_2-am) and upon crystallization in air at different temperatures of 300 (TiO_2-300), 450 (TiO_2-450), and 600 °C (TiO_2-600) are shown in Figure 1.

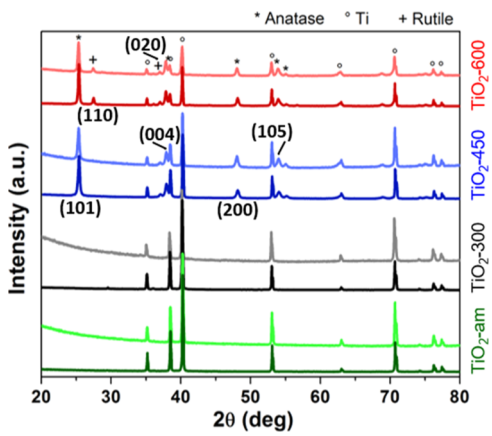

Figure 1. XRD patterns of TiO_2 NTs nonthermally treated and thermally treated at 300, 450, and 600 °C. Dark colors indicate samples before cycling, while light colors refer to cycled electrodes. The growth time by anodic oxidation is kept constant at 5 min.

The TiO_2-am and TiO_2-300 samples show only the Ti reflections (reference JCPDS 89-5009), independently of the NTs length, thus accounting for their bare amorphous characteristics; even if some literature references report the formation of anatase at 300 °C,[58] we did not detect it in our experiments. The formation of an anatase polycrystalline structure is clearly seen in the diffraction pattern of TiO_2-450 and justified by the presence of the peaks related to the (0 0 4), (1 0 1), (1 0 5), and (2 0 0) crystal planes (JCPDS 89-4921). As regards the additional peaks present in the pattern, they originate from the Ti substrate (JCPDS 89-5009). No additional peak is observable, which might be ascribable to some foreign impurity phases. Finally, TiO_2-600 shows both anatase (reference JCPDS 89-4921) and rutile (reference JCPDS 87-0710) (1 1 0) and (0 2 0) peaks, thus accounting for a mixed crystalline phase structure. Indeed, the resulting material of the anodic oxidation process is polycrystalline, and there is no possibility to induce a preferred orientation by acting on the preparation parameters.

DOI: 10.1021/acsomega.8b01117
ACS Omega 2018, 3, 8440−8450

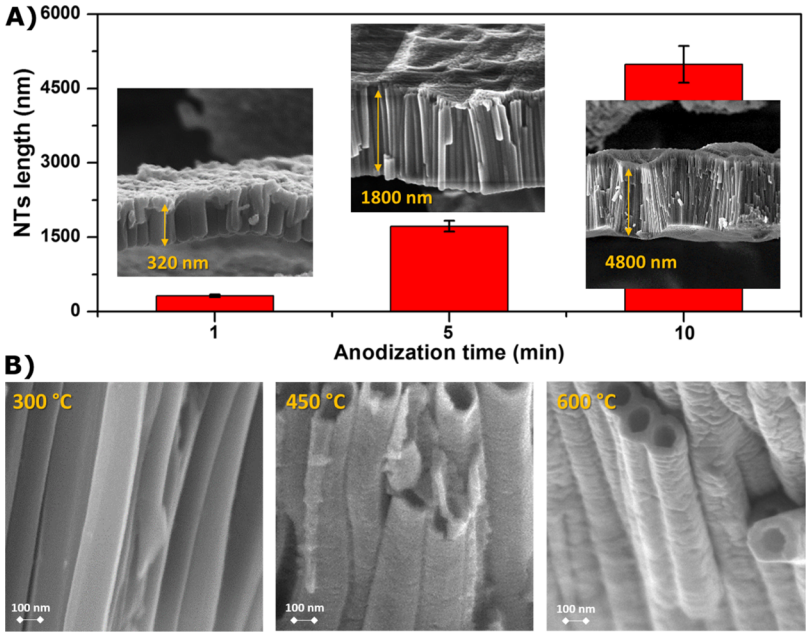

Figure 2. (A) Graph of TiO_2 NTs length vs time of anodization; FESEM images showing different NT lengths are shown as insets. (B) High-magnification FESEM images of the NTs annealed at different temperatures, namely 300, 450, and 600 °C, for 1 h in ambient atmosphere.

The dependency of TiO_2 NTs array length on their electrochemical performance as electrodes in sodium cells was investigated. The length was controlled by acting on the time of anodization during synthesis: Figure 2A shows the expected linear growth of the nanotubes for 1, 5, and 10 min with corresponding FESEM images of the cross sections. The resulting lengths are about 320, 1800, and 4800 nm, respectively.

Moreover, the effect of crystallization was considered as a parameter of interest on the final performance of the materials. Indeed, the as-grown TiO_2 NTs are completely amorphous, but they can be thermally crystallized in the desired polycrystalline phase (anatase, rutile, or mixed phase) by simply selecting the right calcination temperature in ambient atmosphere. The high magnification FESEM images collected in Figure 2B illustrate the morphological evolution of the NTs wall during thermal treatments. Almost no difference can be appreciated up to 300 °C, but at higher calcination temperatures the nanotubes walls start exhibiting some small cracks and an increased roughness due to crystallite formation. In all cases, the TiO_2 nanotube arrays demonstrate excellent mechanical robustness and self-standing ability.

2.2. Electrochemical Characterization in Sodium Cells. The evaluation of the electrochemical behavior in laboratory-scale sodium test cells was carried out at ambient temperature by means of constant current (galvanostatic) discharge/charge cycling at various current regimes, from 0.1 to 5 mA cm^{-2}. It is worth noting that, thanks to their self-supporting ability and excellent mechanical integrity, the TiO_2 NTs arrays supported on the underneath titanium foil were directly assembled in laboratory-scale sodium cells, without any addition of conductivity enhancers and/or binders, thus leading to an increased overall energy density output from the working electrode.

Representative potential versus specific capacity profiles for all the samples under study are shown in Figure 4. They are extracted from the ambient temperature long-term cycling tests obtained at different current regimes between 0.1 and 2.5 V versus Na^+/Na (see Figure 3). The formation of the solid electrolyte interface passivating film at the surface of the

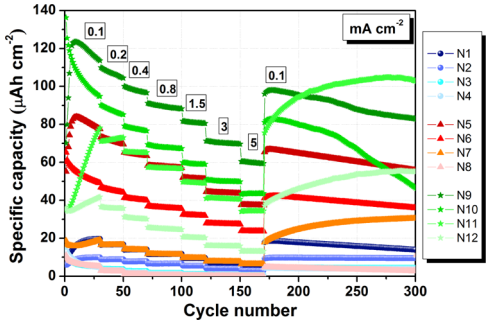

Figure 3. Specific discharge capacity vs cycle number at different current densities (from 0.1 to 5 mA cm^{-2}) for sodium cells assembled with TiO_2 NT arrays as working electrodes, as described in Table 1.

nanotubes is clearly visible in the initial discharge (Na-ion insertion) step as a steadily sloping pseudopotential plateau slightly below 1.0 V versus Na^+/Na (black profile in all the upper plots in Figure 4). It is the main responsible of the initial large irreversible capacity and corresponding low Coulombic efficiency, in agreement with literature reports.[57,59] After the initial irreversible reactions took place, the charge/discharge processes unfold into typical S-type shaped reversible sloping potential profiles, where a visible plateau is not clearly present for both discharge and charge curves, but only the expected gradual evolution associated with a continuous solid-solution reaction between sodium ions and active material, as for the typical behavior of titania upon reversible insertion/de-insertion of sodium ions.[57,60] Overall, the process is highly reversible for all the samples, as well-evidenced by the very similar Na^+ ions insertion/de-insertion capabilities, even when increasing the current regimes. This observation clearly accounts for the lack of structural changes upon reversible reaction with sodium ions and the good diffusion pathways.

DOI: 10.1021/acsomega.8b01117
ACS Omega 2018, 3, 8440−8450

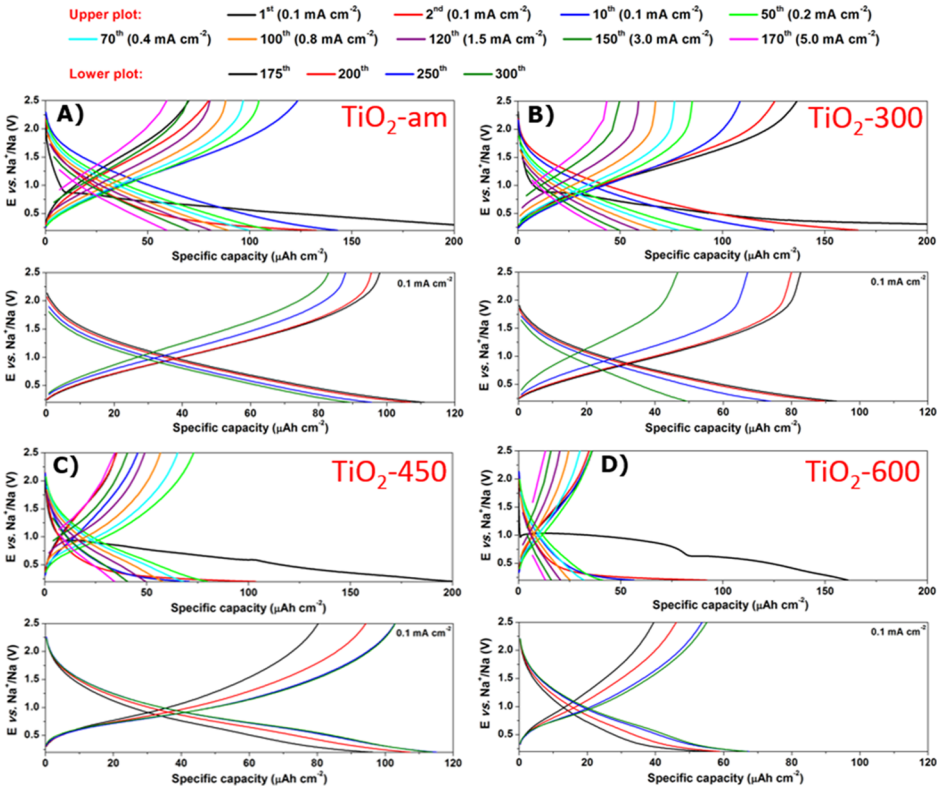

Figure 4. Ambient temperature electrochemical behavior of the different TiO_2 NTs arrays under study: TiO_2-am (A), TiO_2-300 (B), TiO_2-450 (C), and TiO_2-600 (D). In particular, constant-current discharge/charge potential vs specific capacity profiles are shown between cycles 1 and 170 at different current densities from 0.1 to 5 mA cm^{-2} (upper plots in A–D) and between cycles 170 and 300 at fixed 0.1 mA cm^{-2} (lower plots in A–D).

The symmetry and shape of the constant current profiles remain almost unchanged upon cycling, which accounts for the good structural stability of the materials, as also confirmed by XRD analysis after cycling (see Figure 1).

The potential drop at below 0.6 V versus Na^+/Na, which is visible in TiO_2-450 and, particularly, in TiO_2-600, is attributed to the reversible sodiation/desodiation process in rutile TiO_2 host, which is consistent with previous reports.[61,62] The process is visible, even if much reduced, in the following cycles and, in particular, at lower current regimes; this may suggest that the reaction between rutile TiO_2 and Na^+ is a surface-confined charge-transfer process.[63]

The comparison of the constant current profiles of the different samples clearly enlightens that TiO_2-450 and TiO_2-600, calcined at higher temperature, demonstrate a remarkable increase in the specific capacity output at 0.1 mA cm^{-2} and upon long-term cycling (lower plots in Figure 4). This reflects an increased material utilization upon reversible cycling of highly crystalline samples, which is not the case for the materials having a higher degree of amorphicity.

2.3. Nanostructure-Performance Correlation by a Design of Experiments (DoE) Approach. The experimental parameters behind the preparation (and related characteristics) of vertically aligned TiO_2 NTs and the resulting performances in lab-scale sodium cells were investigated by means of a chemometric approach. The proposed multivariate mathematical analysis represents a powerful tool if the aim is that of optimizing functional materials, especially when it is required to determine variables as others are modified in the experimental work. By means of this statistical-mathematical approach, the operational variables (i.e., the growth time of TiO_2 NTs by anodic oxidation and the annealing temperature) can be concurrently varied to identify the relative weight of each one and the relation between them, particularly indicating synergies and antagonisms. This approach aims at challenging the strong imbalance that now exists between the technical ability to generate a large amount of excellent experimental data and the human ability to interpret them properly.

Fourteen sodium cells were assembled to investigate the experimental domain in the proposed chemometric approach. The overall constant-current cycling behavior at various current densities (0.1–5 mA cm^{-2}) of the series of TiO_2 NTs arrays under study is shown in Figure 3, where the influence of the growth time on the overall materials performance as well as the peculiar opposite behavior of amorphous and crystalline TiO_2 NTs samples is well-evidenced. Only specific capacity values upon discharge are plotted to simplify the figure and facilitate the understanding.

The chemometric matrix shown in Table 1 was filled with the experimental responses corresponding to the specific capacity values of the assembled sodium cells at the 85th cycle. The interpolation parameters derived from the multiple linear regression were $Q^2 = 0.79$ (i.e., the fraction of the variation of the response that can be predicted by the model) and $R^2 = 0.95$ (i.e., the fraction of the variation of the response explained by the model). In other words, these parameters provide the summary of the fit for the studied model, representing overestimated (R^2) and underestimated (Q^2) measures of the quality of chemometric model fitting. In the present study, R^2 and Q^2 are close to 1 (R^2 in particular), which indicates that an excellent description of the relationship between the response and the independent variables is provided by the regression

DOI: 10.1021/acsomega.8b01117
ACS Omega 2018, 3, 8440–8450

Table 1. Experimental Matrix of Variables (x_1 = Growth Time of TiO_2 NTs by Anodic Oxidation, x_2 = Annealing Temperature) and Corresponding Experimental and Predicted Responses To Optimize the Specific Capacity of the Samples

cell	x_1 (min)	x_2 (°C)	measured specific capacity (μAh cm^{-2})	predicted specific capacity (μAh cm^{-2})
N1	1	25	11.6	12.3
N2	1	300	6.6	7.9
N3	1	450	1.8	2.1
N4	1	600	1.1	0.3
N5	5	25	57.7	56.4
N6	5	300	36.1	38.9
N7	5	450	11.5	10.8
N8	5	600	0.4	0.8
N9	10	25	89.4	90.9
N10	10	300	67.9	67.0
N11	10	450	57.0	58.0
N12	10	600	25.0	27.2
N13	5	450	11.2	10.8
N14	5	450	12.0	10.8

model; this is also clear when predicted specific capacity values listed in the last column of Table 1 are considered.

The set of experiments permitted the achievement of a maximum specific capacity of 90.9 μAh cm^{-2} for the cell assembled with the amorphous TiO_2-am sample, which was grown for 10 min and clearly not annealed. Figure 5A shows how much each variable influences the experimental response, with 95% confidence. From the coefficient plot shown in this figure, it is possible to write the modeling equation, which represents an empirical relationship between the variables and the response expressed in polynomial form:

$$y = 31.20(\pm 3.44) + 28.60(\pm 3.12)x_1 - 23.10(\pm 2.45)x_2 + 5.80(\pm 0.47){x_1}^2 - 3.40(\pm 0.03){x_2}^2 - 11.80(\pm 0.97)x_1x_2 \quad (1)$$

where y is the specific capacity of the various sodium cells. The numerical values of the coefficients in the equation indicate the importance of each factor in the equation. It is worth noticing that the coefficients of x_1 and x_2 are positive, while those of the respective quadratic effects are one positive and one negative. It means that a slight increase in x_1 and x_2 leads to an increase in specific capacity, but high values of these factors lead to opposite effects on cells performance. Lastly, the interaction term $x_1 \cdot x_2$ is negative, and this indicates that there is absence of synergistic effects between these two variables.

The response surface of the quadratic matrix of 14 experiments is shown in Figure 5B, where the maximum response zone for specific capacity is observed at x_1 = 10 min and x_2 = 25 °C. Two hypotheses were analyzed to validate the chemometric experimental model:

- H_1: a dependency between the variables exists.
- H_0: a dependency between the variables does not exist.

By using the quadratic differences between the results and their average, the Student's t-test was applied, and it gave a probability of 5% for H_0 and of 95% for H_1, therefore corroborating H_1 and underlining that a dependency between the variables exists.

We decided not to stop cell testing at the 85th cycle (although it was already enough to extract information on the most promising electrodes, i.e., those with the growth time of 10 min). Surprisingly, when we resumed the initial current regime (0.1 mA cm^{-2}), we clearly observed the inversion of the behavior of the amorphous and the anatase electrodes. Specifically, as clearly visible in Figure 6A, the samples calcined at 450 °C and above were much more stable upon long-term operation, while the amorphous sample and TiO_2-300 calcined at low-temperature showed a rapid decay of the specific capacity values. This is also clearly detectable from the contour plot shown in Figure 6B, obtained by fitting the DoE at the 250th cycle. The best performance was obtained by anatase titania samples (i.e., calcined at 450 °C, TiO_2-450), which were grown for 10 min.

Summing up, the chemometric approach enabled the following observations on the investigated system. A direct correlation between growth time and specific capacity output of the cell was evidenced: higher specific capacity values were provided by longer TiO_2 NTs, which were also able to retain very long-term cycling stability. It accounted for the high quality and excellent mechanical robustness of the TiO_2 NTs prepared by anodic oxidation in this work. This might be considered as an "expected" result, but it is not trivial: very often, longer 2D nanostructures lack by proper structural stability that causes a rapid performance decay upon prolonged operation.[64,65] As already discussed,[57] TiO_2-am showed an increase of performance in the very initial cycles at low current, which was then followed by a constant capacity decrease at all of the tested current densities. The TiO_2-300 sample showed likely the same cycling behavior. This was independent on the

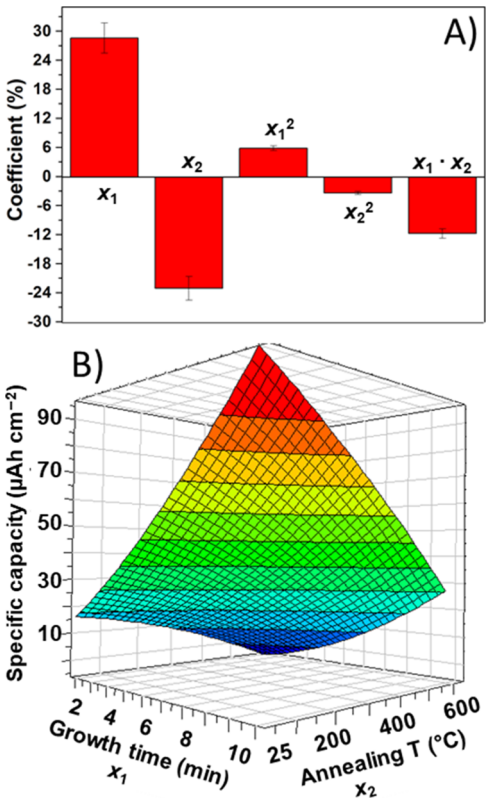

Figure 5. (A) Coefficient plot for the D-optimal DoE; (B) response surface showing the effect of the two experimental parameters on the specific capacity at the 85th cycle of lab-scale sodium cells assembled with the different vertically aligned TiO_2 NTs under study.

DOI: 10.1021/acsomega.8b01117
ACS Omega 2018, 3, 8440−8450

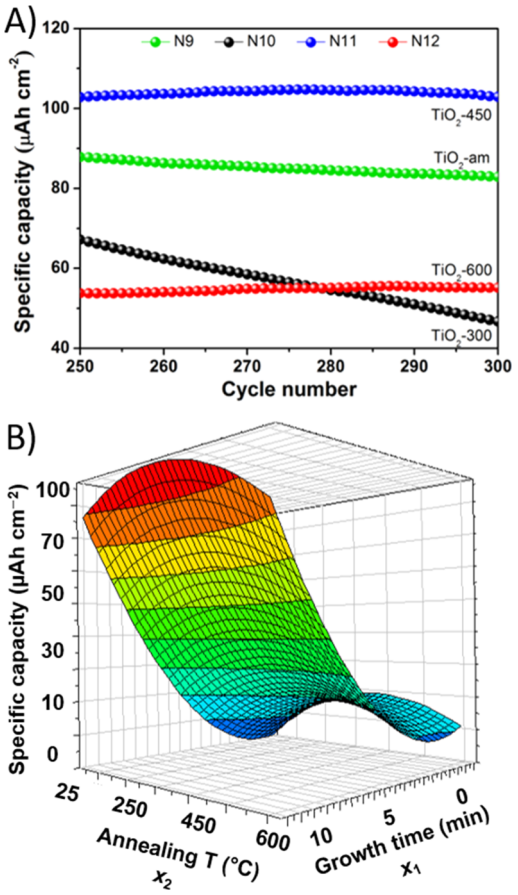

Figure 6. (A) Specific discharge capacity values under 0.1 mA cm^{-2} for sodium cells assembled with TiO_2 NTs array working electrodes (growth time = 10 min) between the 250th and 300th cycle; (B) response surface showing the effect of annealing temperature and growth time on the specific capacity at the 250th cycle of lab-scale sodium cells.

growth time, as both longer and shorter nanotubes had the same behavior. Highly crystalline samples TiO_2-450 and TiO_2-600 showed a rapid specific capacity increase at low current density during initial operation; the specific capacity gain remained constant even at higher current densities. It is worth noting that the specific capacity of the crystalline samples relentlessly and monotonously increased when the current was reduced back to low 0.1 mA cm^{-2}, which is a completely different behavior if compared to amorphous samples. It confirms the superior long-term cycling performance of anatase TiO_2 NTs over their amorphous counterparts. The presence of rutile phase, which was obtained upon calcination at 600 °C, in the material did not influence the overall cycling behavior but was clearly not beneficial to the overall specific capacity output.

2.4. Nanostructure-Performance Correlation by a Theoretical Approach. From the previous sections, a distinction in the performance between anatase, rutile and amorphous TiO_2 clearly emerged. In our previous work,[57] we demonstrated the superior behavior of the anatase phase upon long-term reversible cycling in lab-scale sodium cells. This is confirmed here, as the single-phase anatase polymorph, obtained by calcination at 450 °C, provides the highest specific capacity value after 300 reversible discharge/charge cycles. The growth time also affects the electrochemical response of the material, and, in particular, notwithstanding the calcination temperature, the best results are obtained at longer growth time. In the present work, we also demonstrate that the presence of foreign phases of TiO_2 other than pure anatase negatively affects the electrochemical performance. In this respect, the TiO_2-600 sample shows a sizeable amount of rutile, which is formed upon calcination at 600 °C (see XRD diffraction patterns in Figure 1), thus resulting in a mixed anatase/rutile structure. It shows a substantial decrease in the overall specific capacity output at all of the different current regimes if compared to the single-phase anatase (TiO_2-450), which suggests the limited reversible insertion/de-insertion capability of the rutile polymorph.

To confirm this statement, we have performed state-of-the-art density functional theory (DFT) calculations of Na^+ insertion in TiO_2 rutile bulk phase, following the same approach as for the case of TiO_2 anatase bulk.[57] We employed a 96-atom structural model for TiO_2 rutile, corresponding to a 2 × 2 × 4 supercell. The relaxed structural parameters are in good agreement with the experimental values, as listed in Table 2.

Table 2. DFT-PBE Minimum-Energy Structural Parameters for TiO_2 Rutile Bulk Phase (Space Group No. 136: $P4_2/mnm$), Lattice Vectors ($a = b$, c) in Å and u Coordinate of the 4f Wyckoff Position for the Oxygen

	this work	exp.[a]
$a = b$ (Å)	4.6364	4.5936
c (Å)	2.9862	2.9862
u_O	0.3047	0.3048

[a]Reference 66.

The rutile structure presents a cavity that forms a channel along the [001] direction: in this cavity, it is possible to accommodate a Na^+ cation, as depicted by Figure 7.

The insertion energy has been computed according to the following equation:

$$E_{ins} = E(Na{:}TiO_2) - E(TiO_2) - E(Na_m) \quad (2)$$

where $E(Na{:}TiO_2)$ is the total energy of the system with the inserted Na^+ cation; $E(TiO_2)$ and $E(Na_m)$ are the reference energies for titania and sodium metal, respectively. The computed E_{ins} for the insertion of the first sodium in rutile is 0.988 eV. This positive value means that the insertion is not energetically favorable, and the reason is to be found in the distortions of the Ti_6O_6 cavity that accommodates the sodium: the oxygen−oxygen distances (see d_1 and d_2 Figure 7C) are perturbed by the large Na^+ cation and especially d_1 is elongated by ∼20% to make room for sodium.

The rutile unfavorable insertion energy should be compared to the E_{ins} value of −0.14 eV computed for the anatase phase.[57] We also computed the insertion energies for a second Na^+ cation in different relative positions with respect to the first cation; Figure 8 depicts the different configurations.

The insertion of the second sodium is always unfavorable; the computed insertion energies E_{ins} for the different configurations are (A) 1.379, (B) 1.725, (C) 0.855, and (D) 3.074 eV. These high-energy values correspond to very unfavorable insertion for a second Na^+ cation. For the C configuration, the computed E_{ins} is the least unfavorable, while the most unfavorable is the D configuration where there is a strong displacement of a Ti atom in a TiO_6 moiety in between two insertion sites. These computed values in rutile are much

DOI: 10.1021/acsomega.8b01117
ACS Omega 2018, 3, 8440−8450

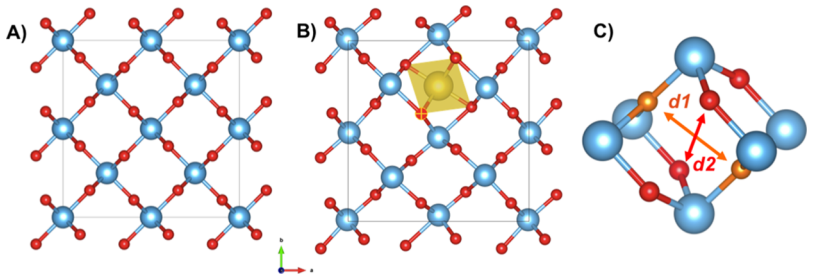

Figure 7. (A) Structural model of the relaxed 96-atom 2 × 2 × 4 supercell of TiO_2 rutile, view along the [001] direction, color code: Ti (cyan) and O (red). (B) Minimum-energy structure for the insertion of a Na^+ cation (yellow) inside the TiO_2 rutile. (C) Zoom over one Ti_6O_6 host "cage" for Na^+ showing six coordination oxygen atoms. The size of this cage is determined by the two closest oxygen atoms (d_1 in orange), while two other equivalent O−O pairs (d_2 in red) lie at a higher distance: d_1 goes from 3.36 Å in pristine TiO_2 rutile to 4.01 Å in the presence of sodium ($Na_{0.03}TiO_2$), and d_2 goes from 4.49 to 4.41 Å.

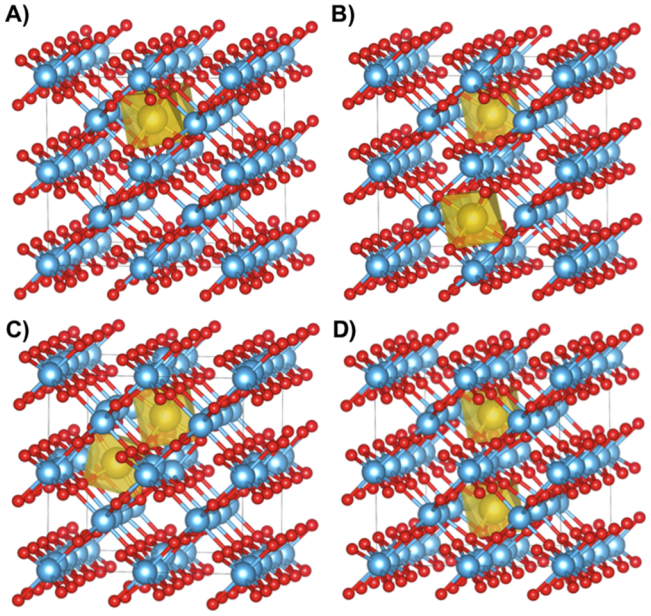

Figure 8. Structural models for a second Na^+ cation placed in different configurations: (A) as next-neighbor along the same [001] channel; (B) in the furthest position within the 96-atom supercell; (C) in an adjacent site of a parallel [001] channel; (D) in a parallel [001] channel bridged by a TiO_6 moiety: the central Ti of such moiety strongly goes off-center upon relaxation. Color code as in Figure 7.

higher than the anatase counterparts, where the computed E_{ins} values for the second sodium are within ∼0.5−0.7 eV.

All these theoretical results support a worsening of Na^+ insertion capability for TiO_2 nanostructures going from anatase to rutile, in agreement with electrochemical experiments. Moreover, these experimental and theoretical results are in agreement with previous observations independently obtained for a different polymorph (TiO_2@C nanospheres) by Wang's group.[67] However, the anodic oxidation process here proposed for nanotubes is faster and cheaper with respect to the hydrothermal method used to design nanospheres by a template approach.

3. CONCLUSIONS

The best nanostructure based on TiO_2 nanotubes as the anode for sodium batteries has been identified by a combined physicochemical, electrochemical, computational, and chemometric approach. The experimental design made it possible to identify anatase electrodes grown for longer anodic oxidation times as the best choice to this purpose, and the DFT study allowed to justify this behavior. Anatase is the most stable polymorph upon cycling, because it is not perturbed by the insertion of new Na ions and the channels directed along the [001] direction guarantee a favorable path for Na ion diffusion. Conversely, the insertion in the rutile structure is not energetically favorable because of the distortions of the Ti_6O_6 cavities that accommodate sodium ions.

The combined approach proposed in this work allowed obtaining a state-of-the-art benchmark as an optimized anode for sodium batteries, an increasingly investigated electrochemical technology for the storage of energy produced from renewable sources. Right now, as the TiO_2 comprises only a small fraction of the Ti foil used, the energy density for full battery cells of size for commercialization will be quite low when considering the mass of the entire cell: a proper choice of Ti foil thickness and an evaluation of its application also in the field of sodium-ion microbatteries will be challenging further steps in this field; alternatively, a thin Ti layer can be deposited onto a standard current collector, subsequently proceeding with the anodization process.

4. EXPERIMENTAL SECTION

4.1. Preparation of Vertically Aligned TiO_2 Nanotubes. TiO_2 nanotube arrays were directly grown on titanium foils (thickness 70 μm, 99.96% purity, Goodfellow) by anodic oxidation. Before use, foils were cleaned by ultrasonication in acetone and soft HF etching (3 wt % HF in aqueous solution for 1 min) to remove the native oxide layer. The electrochemical process was conducted in an electrolytic solution containing NH_4F 0.5 wt % and deionized water 2.5 wt % in ethylene glycol, using a platinum sheet as the counter electrode (thickness 250 μm, 99.99% purity, Goodfellow) at the constant temperature of 25 °C in a Peltier thermostat (LAUDA Omnicool unit 62 Plus) under magnetic stirring. The anodization time was varied in the 1−10 min range applying a constant voltage of 60 V (using a dc power supply, GW Instek SPD-3606) to obtain nanotubes with lengths ranging from approximately 300 nm up to about 5 μm. Samples were then rinsed in distilled water and dried under nitrogen flow. To investigate the effect of the crystallization on the electrochemical performance, the as-grown TiO_2 nanotubes were thermally treated at 300, 450, and 600 °C for 1 h in ambient atmosphere into a laboratory furnace by Abb Furnace Co.

4.2. Chemometric Approach. The first step of our chemometric approach entails the selection of the variables to

DOI: 10.1021/acsomega.8b01117
ACS Omega 2018, 3, 8440−8450

be investigated and their relative experimental domain. In agreement with the purpose of this work, we selected the following experimental variables and related ranges of values: the growth time of TiO_2 NTs by anodic oxidation (x_1, which ranged between 1 and 10 min) and their annealing temperature (x_2, which ranged between 25 °C non-annealed, i.e., amorphous samples, and 600 °C, crystalline samples). The two variables were codified in 3 and 4 levels, respectively.

To carry out a multivariate DoE, the software MODDE (version 11.0.2.2309, Umetrics) was adopted, which is widely used in the chemistry field.[68] An experimental domain as the one considered here can be investigated by means of a D-optimal design, with the goal of achieving the maximum information within a well-determined set of experiments with respect to a stated mathematical model. In detail, if a specified regression model is considered, such as

$$y = X \cdot \beta + \varepsilon \tag{3}$$

where y is a $(N \times 1)$ vector representing the measured responses (i.e., NIB specific capacity), X is a $(N \times p)$ extended design matrix that includes all of the n experiments plus additional columns for the p model terms (e.g., interaction terms, constant term, square terms, etc.), β is a $(p \times 1)$ vector related to coefficients that are unknown and to be determined by fitting the model to the measured responses, ε is a $(N \times 1)$ residuals vector indicating the differences between the predicted and observed values of the response y, and the D-optimal design constitutes the statistical mean that permits the maximization of the $X'X$ matrix determinant, being an overall measure of the information in X.[69]

When chemometrics is adopted in materials chemistry studies, the D-optimal design is typically built up by choosing N experiments (runs) from a candidate set, representing the discrete set of "all potential good experiments" included in the experimental domain that is initially defined by the operator. After this step, the best design is constructed by a selection process that depends on the number of runs that can be carried out by the operator (some experiments can be performed easily, others are costly) and on a statistical criterion. On the basis of our previous experiences in the field, we selected G-efficiency (G_{eff}) as the statistical criterion, which is defined by this mathematical equation

$$G_{eff} = \frac{100 \cdot p}{n \cdot d} \tag{4}$$

where p is the number of terms in the model, n the number of experiments in the design, and d the maximum relative prediction variance over the candidate set. The higher the numerical value of G_{eff} criterion, the higher is the probability to obtain the maximum amount of information from the experimental setup defined with the software and performed in the laboratory. In the present case, the highest value of G_{eff} was obtained for a D-optimal design built with 14 runs, which will be described in the following. A thorough discussion of the mathematical and statistical basis behind the selected DoE can also be found elsewhere.[70] The experimental matrix generated by the software is shown in Table 1. Our selected experimental response (y) was the specific capacity of the lab-scale sodium cells at the 85th galvanostatic cycle, thus having a clear idea about the performance of each device assembled with the TiO_2 NTs electrodes prepared accordingly to the experimental protocol described above.

To evaluate the experimental reproducibility following the standard criteria of DoE techniques, three replicates (named N7, N13, and N14 in Table 1) of the central point were carried out.

4.3. Characterization of the Materials, Fabrication of the Devices, and Electrochemical Tests. The morphology of the as-grown nanotubes was studied by FESEM analysis using a MERLIN ZEISS instrument, equipped with an energy dispersive X-ray spectrometer for compositional analyses. XRD analysis was used to assess the structural characteristics of the materials. A PANalytical X'Pert MRD Pro instrument, equipped with a Cu Kα X-ray source and a curved graphite secondary monochromator, was used to study the samples both before and after galvanostatic cycling.

The electrochemical behavior of the vertically aligned TiO_2 NTs upon reversible insertion/de-insertion of Na^+ ions was studied in three-electrode T-cells made of polypropylene and assembled by contacting in sequence a working electrode (i.e., Ti foil-supported TiO_2 NTs disk, with an area of 20 mm^2), a separator (that was a Whatman Grade GF/A product soaked into a 1.0 M solution of sodium perchlorate—$NaClO_4$ by Solvionic—in propylene carbonate—PC, Solvionic), and a counter electrode (a sodium metal foil by Sigma-Aldrich). $NaClO_4$/PC was selected as the preferred electrolyte solution as we found it to be the most performing in terms of Coulombic efficiency and specific capacity output and is also low cost and easily available.[71]

Constant current (galvanostatic) discharge (Na^+ insertion)/charge (Na^+ de-insertion) cycling was conducted at ambient temperature (≈20 °C) using the battery testing system model BT2000 by Arbin Instruments. Discharge/charge cycles for all the cells were set at the same rate ranging from 0.1 to 5 mA cm^{-2} and keeping a cut off potentials: 0.2−2.5 V versus Na^+/Na. Procedures of devices assembly were carried out under inert and controlled atmosphere by using a GP Dry-Glove Box Workstation by Jacomex (H_2O and O_2 content lower than 0.1 ppm), filled with extra pure Ar 6.0. Before assembly, all samples were prepared and stored in an environmentally controlled dry-room (10 m^2, relative humidity <2% ± 1 at 20 °C) produced by Soimar Group.

4.4. Computational Details. We performed spin-polarized Kohn−Sham DFT[72,73] calculations by means of the generalized-gradient approximation with the exchange−correlation density functional of Perdew, Burke, and Ernzerhof (PBE),[74] as implemented in the VASP code.[75−77] The projector-augmented wave potentials were used to describe nuclei and core electrons.[78,79] The pseudo-wave functions was expanded in a plane-wave basis set with a kinetic energy cut-off of 600 eV and a k-point sampling based on Γ-centered 3 × 3 × 3 grid for the 96-atom TiO_2 2 × 2 × 4 supercell. With these numerical parameters the achieved convergence for total electronic energies is within 5 meV per formula unit. Furthermore, structural optimization were carried out until the convergence of Hellmann−Feynman forces with a threshold of 10 meV $Å^{-1}$.

AUTHOR INFORMATION

Corresponding Authors

*E-mail: federico.bella@polito.it. Phone: +39 0110904643 (F.B.).

*E-mail: claudio.gerbaldi@polito.it (C.G.).

DOI: 10.1021/acsomega.8b01117
ACS Omega 2018, 3, 8440−8450

ORCID

Federico Bella: 0000-0002-2282-9667
Andrea Lamberti: 0000-0003-4100-9661
Michele Pavone: 0000-0001-7549-631X

Notes

The authors declare no competing financial interest.

■ ACKNOWLEDGMENTS

The authors would like to thank Mauro Raimondo for the FESEM analysis of the as-prepared samples. Part of this work was carried out within the activities "Ricerca Sistema Elettrico" funded through contributions to research and development by the Italian Ministry of Economic Development.

■ REFERENCES

(1) Saavedra M, M. R.; de O. Fontes, C. H.; Freires, F. G. M. Sustainable and Renewable Energy Supply Chain: A System Dynamics Overview. *Renewable Sustainable Energy Rev.* **2018**, *82*, 247−259.

(2) Baranes, E.; Jacqmin, J.; Poudou, J.-C. Non-Renewable and Intermittent Renewable Energy Sources: Friends and Foes? *Energy Policy* **2017**, *111*, 58−67.

(3) Goodenough, J. B.; Kim, Y. Challenges for Rechargeable Li Batteries. *Chem. Mater.* **2010**, *22*, 587−603.

(4) Park, J.-k.; Park, G.-g.; Kwak, H. H.; Hong, S. T.; Lee, J.-w. Enhanced Rate Capability and Cycle Performance of Titanium-Substituted P2-Type $Na_{0.67}Fe_{0.5}Mn_{0.5}O_2$ as a Cathode for Sodium-Ion Batteries. *ACS Omega* **2017**, *3*, 361−368.

(5) Wang, K.; Jin, Y.; Sun, S.; Huang, Y.; Peng, J.; Luo, J.; Zhang, Q.; Qiu, Y.; Fang, C.; Han, J. Low-Cost and High-Performance Hard Carbon Anode Materials for Sodium-Ion Batteries. *ACS Omega* **2017**, *2*, 1687−1695.

(6) Chen, Q.; Xu, R.; He, Z.; Zhao, K.; Pan, L. Printing 3D Gel Polymer Electrolyte in Lithium-Ion Microbattery Using Stereolithography. *J. Electrochem. Soc.* **2017**, *164*, A1852−A1857.

(7) Schnell, J.; Günther, T.; Knoche, T.; Vieider, C.; Köhler, L.; Just, A.; Keller, M.; Passerini, S.; Reinhart, G. All-solid-state lithium-ion and lithium metal batteries—paving the way to large-scale production. *J. Power Sources* **2018**, *382*, 160−175.

(8) Long, W.; Fang, B.; Ignaszak, A.; Wu, Z.; Wang, Y.-J.; Wilkinson, D. Biomass-derived Nanostructured Carbons and their Composites as Anode Materials for Lithium Ion Batteries. *Chem. Soc. Rev.* **2017**, *46*, 7176−7190.

(9) Eftekhari, A. Low Voltage Anode Materials for Lithium-Ion Batteries. *Energy Storage Mater.* **2017**, *7*, 157−180.

(10) Li, S.; Mohamed, A. I.; Pande, V.; Wang, H.; Cuthbert, J.; Pan, X.; He, H.; Wang, Z.; Viswanathan, V.; Whitacre, J. F.; Matyjaszewski, K. Single-Ion Homopolymer Electrolytes with High Transference Number Prepared by Click Chemistry and Photoinduced Metal-Free Atom-Transfer Radical Polymerization. *ACS Energy Lett.* **2018**, *3*, 20−27.

(11) Arora, N.; Singh, S.; Kumar, R.; Kumar, R.; Kumari, A. Ionic conductivity, SEM, TGA and rheological studies of Nano-dispersed silica based polymer gel electrolytes containing LiBF4. *Solid State Ionics* **2018**, *317*, 175−182.

(12) Fu, X.; Li, C.; Wang, Y.; Kovatch, L. P.; Scudiero, L.; Liu, J.; Zhong, W. Building Ion-Conduction Highways in Polymeric Electrolytes by Manipulating Protein Configuration. *ACS Appl. Mater. Interfaces* **2018**, *10*, 4726−4736.

(13) Aldalur, I.; Martinez-Ibañez, M.; Piszcz, M.; Rodriguez-Martinez, L. M.; Zhang, H.; Armand, M. Lowering the Operational Temperature of All-Solid-State Lithium Polymer Cell with Highly Conductive and Interfacially Robust Solid Polymer Electrolytes. *J. Power Sources* **2018**, *383*, 144−149.

(14) Zeng, H.; Ji, X.; Tsai, F.; Zhang, Q.; Jiang, T.; Li, R. K. Y.; Shi, H.; Luan, S.; Shi, D. Enhanced cycling performance for all-solid-state lithium ion battery with LiFePO 4 composite cathode encapsulated by poly (ethylene glycol) (PEG) based polymer electrolyte. *Solid State Ionics* **2018**, *320*, 92−99.

(15) Gupta, H.; Kataria, S.; Balo, L.; Singh, V. K.; Singh, S. K.; Tripathi, A. K.; Verma, Y. L.; Singh, R. K. Electrochemical study of Ionic Liquid based polymer electrolyte with graphene oxide coated LiFePO 4 cathode for Li battery. *Solid State Ionics* **2018**, *320*, 186−192.

(16) Singh, S. K.; Shalu; Balo, L.; Gupta, H.; Singh, V. K.; Tripathi, A. K.; Verma, Y. L.; Singh, R. K. Improved Electrochemical Performance of EMIMFSI Ionic Liquid based Gel Polymer Electrolyte with Temperature for Rechargeable Lithium Battery. *Energy* **2018**, *150*, 890−900.

(17) Devaux, D.; Liénafa, L.; Beaudoin, E.; Maria, S.; Phan, T. N. T.; Gigmes, D.; Giroud, E.; Davidson, P.; Bouchet, R. Comparison of single-ion-conductor block-copolymer electrolytes with Polystyrene-TFSI and Polymethacrylate-TFSI structural blocks. *Electrochim. Acta* **2018**, *269*, 250−261.

(18) Fletcher, S. Bottled Lightning: Superbatteries. *Electric Cars, and the New Lithium Economy*; Hill and Wang: New York, 2012.

(19) Zhang, W.; Tu, Z.; Qian, J.; Choudhury, S.; Archer, L. A.; Lu, Y. Design Principles of Functional Polymer Separators for High-Energy, Metal-Based Batteries. *Small* **2018**, *14*, 1703001.

(20) Wu, F.; Yuan, Y.-X.; Cheng, X.-B.; Bai, Y.; Li, Y.; Wu, C.; Zhang, Q. Perspectives for Restraining Harsh Lithium Dendrite Growth: Towards Robust Lithium Metal Anodes. *Energy Storage Mater.* **2018**, *15*, 148−170.

(21) Chen, W.; Yu, H.; Lee, S.-Y.; Wei, T.; Li, J.; Fan, Z. Nanocellulose: A Promising Nanomaterial for Advanced Electrochemical Energy Storage. *Chem. Soc. Rev.* **2018**, *47*, 2837−2872.

(22) Tarascon, J.-M. Is Lithium the New Gold? *Nat. Chem.* **2010**, *2*, 510.

(23) Bloomberg, L. P. Website. https://www.bloomberg.com (accessed March 2018).

(24) Pan, H.; Hu, Y.-S.; Chen, L. Room-Temperature Stationary Sodium-Ion Batteries for Large-Scale Electric Energy Storage. *Energy Environ. Sci.* **2013**, *6*, 2338−2360.

(25) Kundu, D.; Talaie, E.; Duffort, V.; Nazar, L. F. The Emerging Chemistry of Sodium Ion Batteries for Electrochemical Energy Storage. *Angew. Chem., Int. Ed.* **2015**, *54*, 3432−3448.

(26) Song, X.; Li, X.; Bai, Z.; Yan, B.; Xiong, D.; Lin, L.; Zhao, H.; Li, D.; Shao, Y. Rationally-designed configuration of directly-coated Ni 3 S 2 /Ni electrode by RGO providing superior sodium storage. *Carbon* **2018**, *133*, 14−22.

(27) Yabuuchi, N.; Kubota, K.; Dahbi, M.; Komaba, S. Research Development on Sodium-Ion Batteries. *Chem. Rev.* **2014**, *114*, 11636−11682.

(28) Ponrouch, A.; Monti, D.; Boschin, A.; Steen, B.; Johansson, P.; Palacín, M. R. Non-Aqueous Electrolytes for Sodium-Ion Batteries. *J. Mater. Chem. A* **2015**, *3*, 22−42.

(29) Bella, F.; Colò, F.; Nair, J. R.; Gerbaldi, C. Photopolymer Electrolytes for Sustainable, Upscalable, Safe, and Ambient-Temperature Sodium-Ion Secondary Batteries. *ChemSusChem* **2015**, *8*, 3668−3676.

(30) Islam, M. S.; Fisher, C. A. J. Lithium and Sodium Battery Cathode Materials: Computational Insights into Voltage, Diffusion and Nanostructural Properties. *Chem. Soc. Rev.* **2014**, *43*, 185−204.

(31) Colò, F.; Bella, F.; Nair, J. R.; Gerbaldi, C. Light-Cured Polymer Electrolytes for Safe, Low-Cost and Sustainable Sodium-Ion Batteries. *J. Power Sources* **2017**, *365*, 293−302.

(32) Bommier, C.; Ji, X. Electrolytes, SEI Formation, and Binders: A Review of Nonelectrode Factors for Sodium-Ion Battery Anodes. *Small* **2018**, *14*, 1703576.

(33) Zhang, R.; Wang, Y.; Zhou, H.; Lang, J.; Xu, J.; Xiang, Y.; Ding, S. Mesoporous TiO2 nanosheets anchored on graphene for ultra long life Na-ion batteries. *Nanotechnology* **2018**, *29*, 225401.

(34) Li, H.; Wang, K.; Cheng, S.; Jiang, K. Controllable Electrochemical Synthesis of Copper Sulfides as Sodium-Ion Battery Anodes with Superior Rate Capability and Ultralong Cycle Life. *ACS Appl. Mater. Interfaces* **2018**, *10*, 8016−8025.

DOI: 10.1021/acsomega.8b01117
ACS Omega 2018, 3, 8440−8450

(35) Ling, L.; Bai, Y.; Wang, Z.; Ni, Q.; Chen, G.; Zhou, Z.; Wu, C. Remarkable Effect of Sodium Alginate Aqueous Binder on Anatase TiO2 as High-Performance Anode in Sodium Ion Batteries. *ACS Appl. Mater. Interfaces* **2018**, *10*, 5560−5568.
(36) Chen, H.; Zhang, B.; Wang, X.; Dong, P.; Tong, H.; Zheng, J.-c.; Yu, W.; Zhang, J. CNT-Decorated Na3V2(PO4)3 Microspheres as a High-Rate and Cycle-Stable Cathode Material for Sodium Ion Batteries. *ACS Appl. Mater. Interfaces* **2018**, *10*, 3590−3595.
(37) Metrot, A.; Guerard, D.; Billaud, D.; Herold, A. New Results about the Sodium-Graphite System. *Synth. Met.* **1980**, *1*, 363−369.
(38) Ge, P.; Fouletier, M. Electrochemical Intercalation of Sodium in Graphite. *Solid State Ionics* **1988**, *28*−*30*, 1172−1175.
(39) Luo, W.; Shen, F.; Bommier, C.; Zhu, H.; Ji, X.; Hu, L. Na-Ion Battery Anodes: Materials and Electrochemistry. *Acc. Chem. Res.* **2016**, *49*, 231−240.
(40) Tarascon, J.-M. Key Challenges in Future Li-Battery Research. *Philos. Trans. R. Soc., A* **2010**, *368*, 3227−3241.
(41) Kim, S.-W.; Seo, D.-H.; Ma, X.; Ceder, G.; Kang, K. Electrode Materials for Rechargeable Sodium-Ion Batteries: Potential Alternatives to Current Lithium-Ion Batteries. *Adv. Energy Mater.* **2012**, *2*, 710−721.
(42) Wang, L. P.; Yu, L.; Wang, X.; Srinivasan, M.; Xu, Z. J. Recent Developments in Electrode Materials for Sodium-Ion Batteries. *J. Mater. Chem. A* **2015**, *3*, 9353−9378.
(43) Ling, L.; Bai, Y.; Li, Y.; Ni, Q.; Wang, Z.; Wu, F.; Wu, C. Quick Activation of Nanoporous Anatase TiO2 as High-Rate and Durable Anode Materials for Sodium-Ion Batteries. *ACS Appl. Mater. Interfaces* **2017**, *9*, 39432−39440.
(44) Yan, D.; Yu, C.; Zhang, X.; Li, J.; Li, J.; Lu, T.; Pan, L. Enhanced electrochemical performances of anatase TiO 2 nanotubes by synergetic doping of Ni and N for sodium-ion batteries. *Electrochim. Acta* **2017**, *254*, 130−139.
(45) Liu, S.; Luo, Z.; Tian, G.; Zhu, M.; Cai, Z.; Pan, A.; Liang, S. TiO 2 nanorods grown on carbon fiber cloth as binder-free electrode for sodium-ion batteries and flexible sodium-ion capacitors. *J. Power Sources* **2017**, *363*, 284−290.
(46) Xu, Y.; Memarzadeh Lotfabad, E.; Wang, H.; Farbod, B.; Xu, Z.; Kohandehghan, A.; Mitlin, D. Nanocrystalline Anatase TiO2: A New Anode Material for Rechargeable Sodium Ion Batteries. *Chem. Commun.* **2013**, *49*, 8973−8975.
(47) Usui, H.; Yoshioka, S.; Wasada, K.; Shimizu, M.; Sakaguchi, H. Nb-Doped Rutile TiO2: a Potential Anode Material for Na-Ion Battery. *ACS Appl. Mater. Interfaces* **2015**, *7*, 6567−6573.
(48) Kowalski, D.; Kim, D.; Schmuki, P. TiO2 nanotubes, nanochannels and mesosponge: Self-organized formation and applications. *Nano Today* **2013**, *8*, 235−264.
(49) Roy, P.; Berger, S.; Schmuki, P. TiO2 Nanotubes: Synthesis and Applications. *Angew. Chem., Int. Ed.* **2011**, *50*, 2904−2939.
(50) Ni, J.; Fu, S.; Wu, C.; Maier, J.; Yu, Y.; Li, L. Self-Supported Nanotube Arrays of Sulfur-Doped TiO2 Enabling Ultrastable and Robust Sodium Storage. *Adv. Mater.* **2016**, *28*, 2259−2265.
(51) Liu, N.; Häublein, V.; Zhou, X.; Venkatesan, U.; Hartmann, M.; Mačković, M.; Nakajima, T.; Spiecker, E.; Osvet, A.; Frey, L.; Schmuki, P. "Black" TiO2 Nanotubes Formed by High-Energy Proton Implantation Show Noble-Metal-co-Catalyst Free Photocatalytic H2-Evolution. *Nano Lett.* **2015**, *15*, 6815−6820.
(52) Salazar, R.; Altomare, M.; Lee, K.; Tripathy, J.; Kirchgeorg, R.; Nguyen, N. T.; Mokhtar, M.; Alshehri, A.; Al-Thabaiti, S. A.; Schmuki, P. Use of Anodic TiO2Nanotube Layers as Mesoporous Scaffolds for Fabricating CH3NH3PbI3Perovskite-Based Solid-State Solar Cells. *ChemElectroChem* **2015**, *2*, 824−828.
(53) Bella, F.; Lamberti, A.; Bianco, S.; Tresso, E.; Gerbaldi, C.; Pirri, C. F. Floating, Flexible Polymeric Dye-Sensitized Solar-Cell Architecture: The Way of Near-Future Photovoltaics. *Adv. Mater. Technol.* **2016**, *1*, 1600002.
(54) Su, X.; Wu, Q.; Zhan, X.; Wu, J.; Wei, S.; Guo, Z. Advanced Titania Nanostructures and Composites for Lithium Ion Battery. *J. Mater. Sci.* **2012**, *47*, 2519−2534.
(55) Wu, L.; Bresser, D.; Buchholz, D.; Giffin, G. A.; Castro, C. R.; Ochel, A.; Passerini, S. Unfolding the Mechanism of Sodium Insertion in Anatase TiO2Nanoparticles. *Adv. Energy Mater.* **2015**, *5*, 1401142.
(56) Zhou, M.; Xu, Y.; Xiang, J.; Wang, C.; Liang, L.; Wen, L.; Fang, Y.; Mi, Y.; Lei, Y. Understanding the Orderliness of Atomic Arrangement toward Enhanced Sodium Storage. *Adv. Energy Mater.* **2016**, *6*, 1600448.
(57) Bella, F.; Muñoz-García, A. B.; Meligrana, G.; Lamberti, A.; Destro, M.; Pavone, M.; Gerbaldi, C. Unveiling the controversial mechanism of reversible Na storage in TiO2 nanotube arrays: Amorphous versus anatase TiO2. *Nano Res.* **2017**, *10*, 2891−2903.
(58) Binetti, E.; El Koura, Z.; Patel, N.; Dashora, A.; Miotello, A. Rapid hydrogenation of amorphous TiO2 to produce efficient H-doped anatase for photocatalytic water splitting. *Appl. Catal., A* **2015**, *500*, 69−73.
(59) Yan, D.; Yu, C.; Bai, Y.; Zhang, W.; Chen, T.; Hu, B.; Sun, Z.; Pan, L. Sn-doped TiO2 nanotubes as superior anode materials for sodium ion batteries. *Chem. Commun.* **2015**, *51*, 8261−8264.
(60) Lamberti, A.; Garino, N.; Sacco, A.; Bianco, S.; Chiodoni, A.; Gerbaldi, C. As-grown vertically aligned amorphous TiO2 nanotube arrays as high-rate Li-based micro-battery anodes with improved long-term performance. *Electrochim. Acta* **2015**, *151*, 222−229.
(61) Chen, J.; Zou, G.; Hou, H.; Zhang, Y.; Huang, Z.; Ji, X. Pinecone-like hierarchical anatase TiO2 bonded with carbon enabling ultrahigh cycling rates for sodium storage. *J. Mater. Chem. A* **2016**, *4*, 12591−12601.
(62) He, H.; Sun, D.; Zhang, Q.; Fu, F.; Tang, Y.; Guo, J.; Shao, M.; Wang, H. Iron-Doped Cauliflower-Like Rutile TiO2 with Superior Sodium Storage Properties. *ACS Appl. Mater. Interfaces* **2017**, *9*, 6093−6103.
(63) González, J. R.; Alcántara, R.; Nacimiento, F.; Ortiz, G. F.; Tirado, J. L. Microstructure of the epitaxial film of anatase nanotubes obtained at high voltage and the mechanism of its electrochemical reaction with sodium. *CrystEngComm* **2014**, *16*, 4602−4609.
(64) Sennu, P.; Kim, H. S.; An, J. Y.; Aravindan, V.; Lee, Y.-S. Synthesis of 2D/2D Structured Mesoporous Co3O4Nanosheet/N-Doped Reduced Graphene Oxide Composites as a Highly Stable Negative Electrode for Lithium Battery Applications. *Chem.—Asian J.* **2015**, *10*, 1776−1783.
(65) Fédèle, L.; Sauvage, F.; Gottis, S.; Davoisne, C.; Salager, E.; Chotard, J.-N.; Becuwe, M. 2D-Layered Lithium Carboxylate Based on Biphenyl Core as Negative Electrode for Organic Lithium-Ion Batteries. *Chem. Mater.* **2017**, *29*, 546−554.
(66) Cromer, D. T.; Herrington, K. The Structures of Anatase and Rutile. *J. Am. Chem. Soc.* **1955**, *77*, 4708−4709.
(67) Su, D.; Dou, S.; Wang, G. Anatase TiO2: Better Anode Material Than Amorphous and Rutile Phases of TiO2 for Na-Ion Batteries. *Chem. Mater.* **2015**, *27*, 6022−6029.
(68) Miccoli, B.; Cauda, V.; Bonanno, A.; Sanginario, A.; Bejtka, K.; Bella, F.; Fontana, M.; Demarchi, D. One-Dimensional ZnO/Gold Junction for Simultaneous and Versatile Multisensing Measurements. *Sci. Rep.* **2016**, *6*, 29763.
(69) MODDE 9 User Guide. http://www.umetrics.com (accessed Jan 2018).
(70) de Aguiar, P. F.; Bourguignon, B.; Khots, M. S.; Massart, D. L.; Phan-Than-Luu, R. D-Optimal Designs. *Chemom. Intell. Lab. Syst.* **1995**, *30*, 199−210.
(71) Wu, L.; Buchholz, D.; Bresser, D.; Gomes Chagas, L.; Passerini, S. Anatase TiO2 nanoparticles for high power sodium-ion anodes. *J. Power Sources* **2014**, *251*, 379−385.
(72) Hohenberg, P.; Kohn, W. Inhomogeneous Electron Gas. *Phys. Rev.* **1964**, *136*, B864−B871.
(73) Kohn, W.; Sham, L. J. Self-Consistent Equations Including Exchange and Correlation Effects. *Phys. Rev.* **1965**, *140*, A1133−A1138.
(74) Perdew, J. P.; Burke, K.; Ernzerhof, M. Generalized Gradient Approximation Made Simple. *Phys. Rev. Lett.* **1996**, *77*, 3865−3868.

DOI: 10.1021/acsomega.8b01117
ACS Omega 2018, 3, 8440−8450

(75) Kresse, G.; Hafner, J. Ab initiomolecular dynamics for open-shell transition metals. *Phys. Rev. B: Condens. Matter Mater. Phys.* **1993**, *48*, 13115−13118.
(76) Kresse, G.; Furthmüller, J. Efficient iterative schemes forab initiototal-energy calculations using a plane-wave basis set. *Phys. Rev. B: Condens. Matter Mater. Phys.* **1996**, *54*, 11169−11186.
(77) Kresse, G.; Furthmüller, J. Efficiency of Ab-Initio Total Energy Calculations for Metals and Semiconductors Using a Plane-Wave Basis Set. *Comput. Mater. Sci.* **1996**, *6*, 15−50.
(78) Blöchl, P. E. Projector Augmented-Wave Method. *Phys. Rev. B: Condens. Matter Mater. Phys.* **1994**, *50*, 17953−17979.
(79) Kresse, G.; Joubert, D. From Ultrasoft Pseudopotentials to the Projector Augmented-Wave Method. *Phys. Rev. B: Condens. Matter Mater. Phys.* **1999**, *59*, 1758−1775.

DOI: 10.1021/acsomega.8b01117
ACS Omega 2018, 3, 8440−8450